Fluorescence endomicroscopy with structured illumination

Nenad Bozinovic, Cathie Ventalon, Tim Ford, Jerome Mertz

Department of Biomedical Engineering, Boston University,
44 Cummington St., Boston, MA 02215
nesa@bu.edu, jmertz@bu.edu

Abstract: We present an endomicroscope apparatus that utilizes structured illumination to produce high resolution ($\sim 2.6\mu$m) optically sectioned fluorescence images over a field of view of about 240μm. The endomicroscope is based on the use of a flexible imaging fiber bundle with a miniaturized objective. We also present a strategy to largely suppress structured illumination artifacts that arise when imaging in thick tissue that exhibits significant out-of-focus background. To establish the potential of our endomicroscope for preclinical or clinical applications, we provide images of fluorescein-labeled rat colonic mucosa.

OCIS codes: (180.1790) Microscopy : Confocal microscopy; (180.2520) Microscopy : Fluorescence microscopy; (180.6900) Microscopy : Three-dimensional microscopy.

References and links

1. B. Flusberg, E. Cocker, W. Piyawattanametha, J. Jung, E. Cheung, M. Schnitzer, "Fiber-optic fluorescence imaging", Nat. Meth. 2, 941-950 (2005).
2. L. Giniunas, R. Juškaitis, S. V. Shatalin, "Scanning fiber-optic microscope", Electron. Lett. 27, 724-726 (1991).
3. P. M. Delaney, M. R. Harris, R. G. King, "Fiber-optic laser scanning confocal microscope suitable for fluorescence imaging", Appl. Opt. 33, 573-577 (1994).
4. D. L. Dickensheets and G. S. Kino, "Micromachined scanning confocal microscope", Opt. Lett. 21, 764-766 (1996).
5. L. D. Swindle, S. G. Thomas, M. Freeman, P. M. Delaney, "View of normal human skin in vivo as observed using fluorescent fiber-optics confocal microscopic imaging", J. Invest. Dermatol. 121, 706-712 (2003).
6. T. Ota, H. Fukuyama, Y. Ishihara, H. Tanaka, T. Takamatsu, "In situ fluorescence imaging of organs through compact scanning head for confocal laser microscopy", J. Biomed. Opt. 10, 1-4 (2005).
7. H.-J. Shin, M. C. Pierce, D. Lee, H. Ra, O. Solgaard, R. Richards-Kortum, "Fiber-optic confocal microscope using MEMS scanner and miniature objective lens", Opt. Express 15, 9113-9122 (2007).
8. J. T. C. Liu, M. J. Mandella, H. Ra, L. K. Wong, O. Solgaard, G. S. Kino, W. Piyawattanametha, C. H. Contag, T. D. Wang, "Miniature near-infrared dual-axes confocal microscope utilizing two-dimensional microelectromechanical systems scanner", Opt. Lett. 32, 256-258 (2007).
9. J. Knittel, L. Schneider, L. Buess, G. Messerschmidt, T. Possner, "Endoscope compatible confocal microscope using a gradient index lens system", Opt. Commun. 188, 267-273 (2001).
10. J. C. Jung, A. D. Mehta, E. Aksay, R. Stepnoski, M. J. Schnitzer, "In vivo mammalian brain imaging using one- and two-photon fluorescence microendoscopy", J. Neurophys. 92, 3121-3133 (2004).
11. P. Kim, M. Puoris'haag, D. Coté, C. P. Lin, S. H. Yun, "In vivo confocal and multiphoton microendoscopy", J. Biomed. Opt. 13, 010501 (2008).
12. A. F. Gmitro and D. Aziz, "Confocal microscopy through a fiber optic imaging bundle", Opt. Lett. 18, 565-567 (1993).
13. A. R. Rouse and A. F. Gmitro, "Multispectral imaging with a confocal microendoscope", Opt. Lett. 25, 1708-1710 (2000).
14. C. Liang, K.-B. Sung, R. R. Richards-Kortum, M. R. Descour, "Design of a high-numerical aperture miniature microscope objective for an endoscope fiber confocal reflectance microscope", Appl. Opt. 41, 4603-4610 (2002).
15. E. Laemmela et al, "Fibered Confocal Fluorescence Microscopy (Cell-viZio™) Facilitates Extended Imaging in the Field of Microcirculation", J Vasc Res 41, 400–411 (2004).

16. K. Carlson, M. Chidley, K.-B. Sung, M. Descour, A. Gillenwater, M. Follen, R. Richards-Kortum, "In vivo fiber-optic confocal reflectance microscope with an injection-molded plastic miniature lens", Appl. Opt. 44, 1792-1797 (2005)
17. F. Jean, G. Bourg-Heckly, B. Viellerobe, "Fibered confocal spectroscopy and multicolor imaging system for in vivo fluorescence analysis", Opt. Express 15, 4008-4017 (2007).
18. M.A.A Neil, R. Juškaitis, T. Wilson, "Method of obtaining optical sectioning by using structured light in a conventional microscope", Opt. Lett., Vol. 22, No. 24, (1997).
19. D. Karadaglic, R. Juskaitis, T. Wilson, "Confocal Endoscopy via Structured Illumination", Scanning 24, 301-304 (2002).
20. M.A.A Neil, R. Juškaitis, T. Wilson, "Real time 3D fluorescence microscopy by two beam interference illumination", Opt. Commun. 153, 1-4 (1998).
21. M.A.A Neil et al., "Wide field optically sectioning fluorescence microscopy with laser illumination", J. Micros. 197 Pt1, 1-4 (2000)
22. F. Chasles, B. Dubertret, A. C. Boccara, "Optimization and characterization of a structured illumination microscope", Opt. Express 15, 16130-16140 (2007).
23. M.J. Cole et al, "Time-domain whole-field fluorescence lifetime imaging with optical sectioning", J. Micros. 203, 246-257 (2001).
24. L. H. Schaefer, D. Schuster, J. Schaffer, "Structured illumination microscopy: artefact analysis and reduction utilizing a parameter optimization approach", J. Microsc. 216, 165-174 (2004).
25. H. Fujii, T. Asakura, Y. Shindo, "Measurement of surface roughness properties by using image speckle contrast", J. Opt. Soc. Am. 66, 1217-1222 (1976).
26. E. Jakeman and W. T. Welford, "Speckle statistics in imaging systems", Opt. Commun. 21, 72-79 (1977).
27. K. Ouchi, "Statistics of image plane speckle", Opt. and Quant. Electron. 12, 237-243 (1980).
28. C. Ventalon, R. Heintzmann, J. Mertz, "Dynamic speckle illumination microscopy with wavelet prefiltering", Opt. Lett. 32, 1417-1419 (2007).

1. Introduction

While confocal fluorescence microscopy provides exquisite sub-cellular resolution, it remains limited essentially to surface imaging. To enable access to internalized in-vivo tissue structures in their natural environment, considerable research has been devoted to the implementation of confocal fluorescence microscopy in an endoscopy configuration. Indeed, confocal endomicroscopy promises to become an essential tool for biomedical imaging, both for basic research and in the clinic.

To date, several strategies have been adopted to perform confocal endomicroscopy, which may be separated into two basic categories [1]. In the first category, a single light conduit (typically an optical fiber) delivers illumination to the specimen, and confocal scanning is performed at the distal (specimen) end of the conduit using some kind micromechanical device [2, 3, 4, 5, 6, 7, 8]. Alternatively, in the second category, confocal scanning is performed at the proximal end of the light conduit. In various implementations of this second category, the light conduit has been a rigid gradient-index (GRIN) lens [9, 10, 11] or a flexible imaging fiber bundle [12, 13, 14, 15, 16, 17]. The advantage of proximal scanning is that it obviates the need for precision moving parts at the distal end of the conduit, facilitating miniaturization and robustness. The advantage of using an imaging fiber bundle for a light conduit is that it is flexible and can be quite long, making it particularly amenable to clinical endoscopy applications.

In this paper, we present an implementation of fluorescence endomicroscopy with a flexible fiber bundle that makes use of an imaging technique called structured illumination microscopy (SIM) [18], which is well known to provide confocal-like out-of-focus background rejection without the need for beam scanning. SIM is conceptually simple, highly robust, and can be readily implemented in any widefield imaging device. SIM has already been employed in a rigid Hopkins-type endoscope configuration [19], but to our knowledge a flexible fiber optic version has not yet been demonstrated. In this paper, we present fiber optic version of SIM endomicroscopy, as well as a discussion of imaging artifacts and a strategy to mitigate these artifacts. The purpose of this paper is to establish the potential of SIM endomicroscopy for future intravital imaging. To this end we specifically demonstrate imaging of mouse colonic

mucosa.

2. Endomicroscope setup

Structured illumination microscopy [18] is based on the illumination of a sample with a periodic light pattern, in our case, a one-dimensional grid pattern. Three fluorescence images of the sample are taken at three different grid positions, each laterally translated a third of the grid period. A final optically-sectioned image $I_{\mathrm{SIM}}(x)$ is then generated by the simple algorithm

$$I_{\mathrm{SIM}}(x) = \frac{1}{3\sqrt{2}}\sqrt{(I_1(x)-I_2(x))^2+(I_2(x)-I_3(x))^2+(I_3(x)-I_1(x))^2}. \quad (1)$$

where $I_1(x)$, $I_2(x)$ and $I_3(x)$ are the three raw images, and x is a 2D coordinate in the imaging plane.

The basic idea in constructing a SIM endomicroscope is to make use of an imaging fiber bundle to serve as a relay that guides both the illumination grid pattern to the specimen and the resulting fluorescence distribution back to a CCD camera. A schematic of our setup is illustrated in Fig. 1.

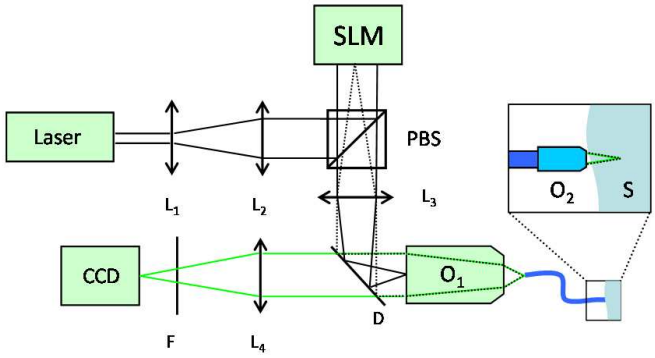

Fig. 1. Endoscope setup. A grid pattern is produced by a spatial light modulator (SLM) and projected onto a sample via an imaging fiber bundle equipped with a miniaturized objective (O_2). The fluorescence generated from the sample is then imaged through this fiber bundle onto CCD camera. Notation: lenses (L), spatial light modulator (SLM), polarizing beam splitter (PBS), dichroic (D), objectives (O), sample (S), filter (F).

Various strategies have been implemented for the application and translation of a grid pattern [21, 20, 22]. In our case, we generate a grid pattern with a liquid crystal spatial light modulator (SLM: Holoeye LC-R 768). The beam from a solid-state diode laser (Cobolt Calypso, $\lambda = 491$nm) is expanded and projected onto the SLM and reflected through a polarizing beamsplitter, allowing the SLM to be operated in an amplitude-modulation mode. In this manner, an arbitrary amplitude pattern can by imparted on the beam profile by computer control of the SLM. In our case, this is a rectangular grid pattern of user-defined period and phase, controlled by Labview software. The pattern is then imaged onto the proximal end of the imaging fiber bundle by way of a lens and microscope objective (Olympus, $20\times$, NA $= 0.4$) producing a net demagnification of $13\times$. The main advantage of an SLM is that it allows us to very conveniently vary our grid period and phase. It is limited in speed, however, providing a maximum effective refresh rate of about 10 Hz, and ultimately leading to a net SIM frame rate of about 2 Hz.

The imaging fiber bundle itself consists of 30,000 cores, each one approximately 1.9μm in diameter separated by an average distance of 3.3μm. The total useful diameter of the fiber bundle is 600μm. A water-immersion miniaturized objective (Mauna Kea Technologies) was optically cemented onto the distal end of the fiber, projecting an image of this distal end into the sample with a demagnification of about $2.5\times$, yielding a field of view of about 240μm. The working distance of this miniaturized objective is 60μm and the NA is about 0.8.

Finally, the fluorescence from the sample is guided back to the proximal end of the fiber bundle and then imaged onto a CCD camera (QImaging Retiga XR) with a magnification of $13\times$. A dichroic (Chroma Z488RDC) and emission filter (Chroma $525/50$m) are used to spectrally isolate the fluorescence.

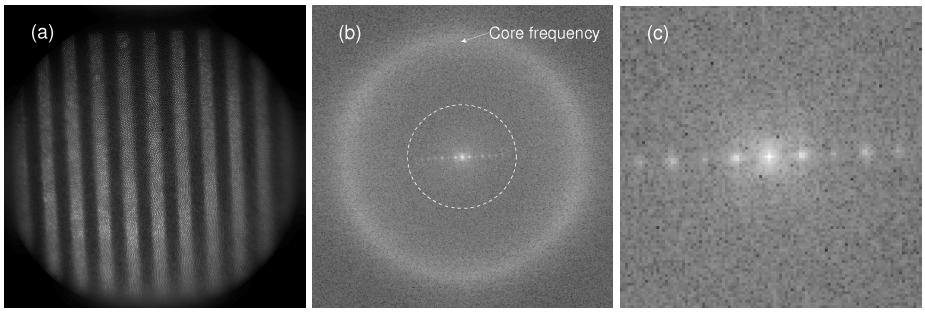

Fig. 2. (a) Raw image of a thin uniform fluorescent sample illuminated with a rectangular grid pattern. (b) Corresponding Fourier transform of this raw image (log brightness scale). The outer ring of frequencies stems from the quasi-periodic distribution of the fiber cores. The inner dashed line is the effective cutoff frequency according to the Nyquist theorem. (c) Blowup of the Fourier transform about the origin. The characteristic harmonics of the grid pattern are apparent.

Figure 2 depicts a raw image of a thin, uniform fluorescent plane illuminated with a grid pattern, as well as 2D Fourier transforms of this image. Two main features are of note in Fig. 2b. The diffuse ring is the result of the quasi-periodic spacing of the cores in the fiber bundle and the inner feature centered about the origin (dc frequency) corresponds to the fluorescence pattern produced by the sample. A blow-up of this feature is illustrated in the Fig. 2c to highlight both a strong dc component and sidebands. The strongest sidebands immendiately to the left and right of dc correspond to the grid fundamental frequency. The additional sidebands correspond to higher harmonics that arise from our use of a rectangular grid pattern.

Fluorescence imaging in our endomicroscope is performed in two steps, a first step from the object plane in the distal fiber bundle plane, and a second step from the proximal fiber bundle plane to the CCD camera. The first step is found to be the most limiting in terms of optical resolution, and from a calculation based on the NA of the distal miniobjective one might expect an optical resolution of about 0.3μm. However, such a resolution cannot be attained with our system because the fluorescence image is sampled by the fiber cores. The quasi-periodic sampling frequency of these cores is clearly apparent as a diffuse ring in Fig 2b. In effect, this sampling frequency restricts the imaging bandwidth of our endomicroscope to an associated Nyquist frequency equal to half this sampling frequency, as depicted by the dashed circle in Fig 2b. Frequency components in our raw images that lie beyond this Nyquist cutoff contain no information about the sample (at least none that can be readily exploited), and we remove these by systematically applying a Gaussian low-pass filter to all our raw images of approximately the same bandwidth as the Nyquist cutoff. That is, we remove the apparent discretization of our images due to the fiber core spacing.

3. SIM imaging

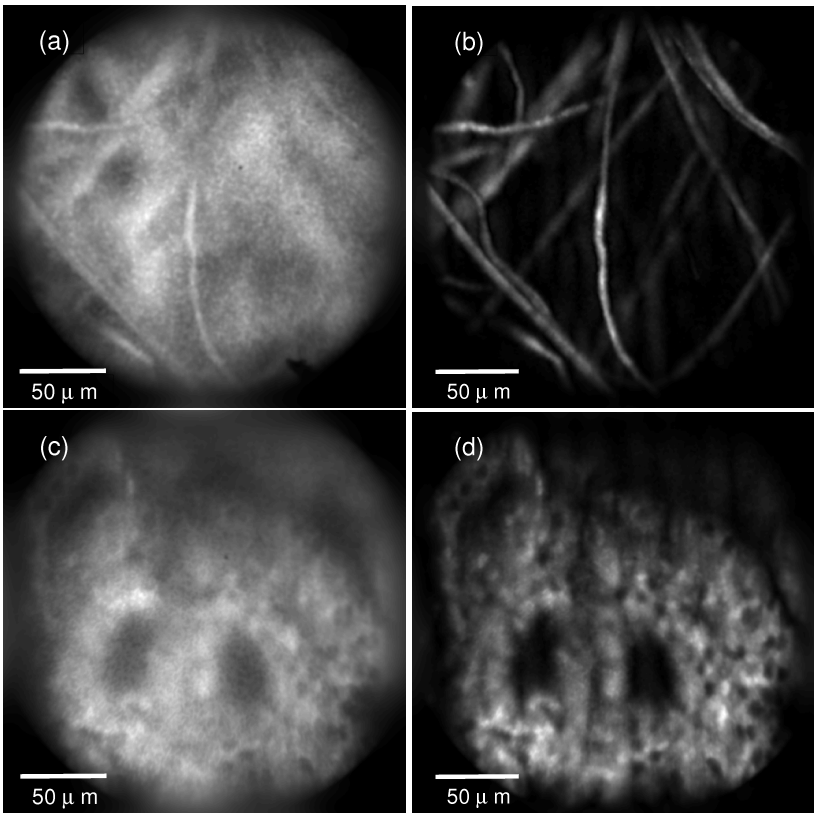

Fig. 3. (a and b) Widefield and SIM image of lens-cleaning paper labeled with a drop of fluorescein solution. (c and d) Widefield and SIM image of an exteriorized rat colonic mucosa labeled with BCECF-AM dye. Artifacts at the grid period (21μm) are apparent in both SIM images.

To test our SIM endomicroscope, we imaged a simple sample comprising lens paper labeled with a small drop of fluorescein solution. The resulting images are illustrated in Fig. 3a. What is referred to as a widefield image is the average of the three raw images I_1, I_2 and I_3, roughly corresponding to the non-sectioned fluorescence image that would be occasioned without the use of SIM. A reduction in fluorescence background is manifestly apparent when the images are processed by the SIM algorithm (Eq. 3). In acquiring these images, a grid frequency of 12% of the Nyquist frequency was used, corresponding to a grid period of 21μm at the sample. This frequency is considerably lower than that prescribed for an optimal sectioning strength [22], however higher grid frequencies proved difficult to faithfully project into the sample because of their greater susceptibility to inaccuracies due to fiber core discretization. Based on the theoretical analysis provided in Ref. [18], the FWHM of our axial sectioning profile with this grid period is estimated to be about 15μm.

A second biologically relevant example is presented in Fig. 3. Mouse colonic mucosa was exteriorized, following mouse sedation and non-survival laparotomy. The colonic mucosa was stretched and loaded luminally with 10μM BCECF-AM dye (Invitrogen) for 10 minutes at room temperature. Endomicroscope imaging was then performed without (Fig. 3c) and with (Fig. 3d) the use of SIM. In the latter case, the out-of-focus background is significantly reduced

and tissue features including surface cells, goblet cells, and dye along the long axis of the crypts become readily apparent.

However Figs. 3b and 3d underscore a common drawback of SIM. In particular, residual grid patterns remain clearly visible in the SIM images. From our experience, such residual grid patterns can be particularly severe when imaging thick scattering samples or when imaging with high grid pattern frequencies. We turn our attention to these artifacts as well as some possible strategies to mitigate them.

4. Artifact reduction

The problem of residual grid patterns in SIM microscopy has been well appreciated [23, 24]. In particular, several causes have been identified for these artifacts, including non-sinusoidal pattern illumination and inaccurate phase shifting. Other causes can be temporal fluctuations in the illumination power or in the fluorescence response (e.g. as a result of photobleaching). In either case, spurious variations between raw images that are not related to the grid pattern. These are not properly rejected by Eq. 3 and ultimately lead to artifacts in the final SIM image. A partial solution to this problem of temporal power fluctuations was proposed in Ref. [23] which consists in normalizing each raw image to its mean prior to processing with Eq. 3. An alternative approach was introduced in Ref. [24] based on the minimization of artifacts by an optimization of several parameters including corrections to illumination power fluctuations and inaccurate phase shifting. This optimization approach, however, is computationally intensive and slow (at least in our hands). Moreover, we have found that it can lead to artifacts of its own.

We present yet another alternative strategy for removing residual grid patterns based on our observation that the residual patterns are more prevalent when imaging thick scattering samples. To understand this strategy, it is useful to revisit Eq. 3, however this time in the Fourier domain.

To begin, it is well known that Eq. 3 is mathematically equivalent to the algorithm [18]

$$I_{\mathrm{SIM}}(x) = \frac{1}{3}\left|I_1(x) + I_2(x)e^{i\frac{2\pi}{3}} + I_3(x)e^{i\frac{4\pi}{3}}\right| \tag{2}$$

This may be recast in the form

$$I_{\mathrm{SIM}}(x) = \left|\mathrm{FT}^{-1}\left[\mathscr{I}_\phi(k)\right]\right| \tag{3}$$

where FT^{-1} corresponds to an inverse Fourier transform and

$$\mathscr{I}_\phi(k) = \frac{1}{3}\left(\mathscr{I}_1(k) + \mathscr{I}_2(k)e^{i\frac{2\pi}{3}} + \mathscr{I}_3(k)e^{i\frac{4\pi}{3}}\right) \tag{4}$$

where $\mathscr{I}_1(k)$, $\mathscr{I}_2(k)$ and $\mathscr{I}_3(k)$ correspond to the Fourier transforms of $I_1(x)$, $I_2(x)$ and $I_3(x)$ respectively. We refer to Eq. 4 as a phase stepping algorithm. Note the absence of an absolute value in Eq. 4 indicating that $\mathscr{I}_\phi(k)$ is complex in general.

Let us first imagine a fluorescent sample that is thin and perfectly in focus. When imaging such a sample with SIM, then $I_1(x)$, $I_2(x)$ and $I_3(x)$ are raw fluorescence images that each exhibit an intensity modulation at the grid-pattern frequency, though phase-shifted between images. Because the sample here is defined to be in focus, the contrast of this modulation can be assumed to be reasonably high (provided the grid frequency k_g is much smaller than the cutoff frequency of the system optical transfer function (OTF)). As a result, if the grid pattern is sinusoidal, then $\mathscr{I}_1(k)$, $\mathscr{I}_2(k)$ and $\mathscr{I}_3(k)$ each contain three components. The first component is the Fourier transform of the unmodulated sample structure centered about $k = 0$ (dc). The second and third components are the same Fourier transform of the sample structure but centered about the sideband frequencies $k = \pm k_g$ and somewhat attenuated by the OTF. The principle of SIM relies on isolating the sample structure in a single sideband. This isolation

cannot be achieved by simple one-sided filtering because of the overlap of the sidebands with themselves and with the unmodulated sample structure. However this isolation can be achieved by phase stepping. That is, the effect of the phase stepping algorithm (Eq. 4) is to remove both the unmodulated (dc) component and a single sideband component, while preserving the other sideband component.

Let us now imagine that this same thin fluorescent sample is displaced far out of focus. Because the OTF severely attenuates high spatial frequencies, then $\mathscr{I}_1(k)$, $\mathscr{I}_2(k)$ and $\mathscr{I}_3(k)$ exhibit only narrow frequency components centered about $k = 0$, regardless of the grid pattern modulation. That is, the grid pattern is so blurred as to play no role. In this case, the effect of applying a phase stepping algorithm, since it removes unmodulated sample structure, is to force $\mathscr{I}_\phi(k)$ to vanish. This is the well-known principle of SIM that leads to out-of-focus background rejection. It should be noted, however, that if the phase stepping is inaccurate in any way, then the unmodulated sample structure is not fully rejected.

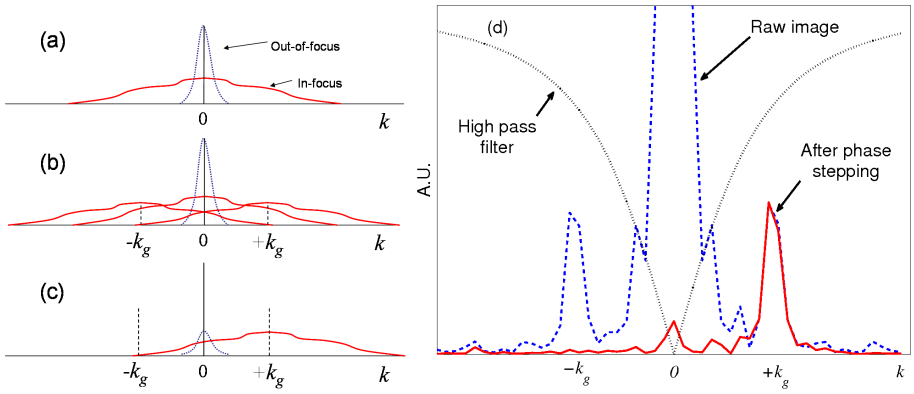

Fig. 4. (a) Schematic illustration of in-focus (red) and out-of-focus (blue dashed) contributions to the intensity spectrum of a widefield image. (b) In-focus and out-of-focus contributions to the intensity of a raw image with grid pattern illumination ($|\mathscr{I}_1(k)|$). Note: only the in-focus contribution becomes modulated. (c) Phase stepping ($\left|\mathscr{I}_\phi(k)\right|$) suppresses both the unmodulated contributions (in-focus and out-of-focus) as well as a single sideband of the modulated contributions (here, left sideband). Imperfect phase stepping leaves behind a residual peak about $k = 0$ (blue dashed) that arises dominantly from the out-of-focus background. (d) Experimental results derived from the sample in Fig. 3d. The intensity spectrum (magnitude) of a single raw image with grid pattern illumination (blue dashed) is plotted alongside the intensity spectrum after phase stepping (red). In the latter case, a residual peak about $k = 0$ is readily apparent. This peak can be rejected with the use of a high pass filter (black dotted).

In practice, when imaging a thick sample, then $\mathscr{I}_1(k)$, $\mathscr{I}_2(k)$ and $\mathscr{I}_3(k)$ contain both in-focus and out-of-focus frequency components. These are schematically illustrated before (Fig. 4a) and after (Fig. 4b) the application of grid illumination, where, again, only the in-focus component is observed to be spatially modulated in the latter case. Figure 4c illustrates the result of phase stepping, where we have introduced a slight inaccuracy that leads to an imperfect rejection of the out-of-focus background, and hence to a spurious peak in $\left|\mathscr{I}_\phi(k)\right|$ in the vicinity of $k = 0$. Our hypothesis of inaccurate phase stepping is borne out in experiment (Fig. 4d) where $|\mathscr{I}_1(k)|$ is illustrated before phase stepping and $\left|\mathscr{I}_\phi(k)\right|$ is illustrated after phase stepping. A spurious peak about $k = 0$ is readily apparent in $\left|\mathscr{I}_\phi(k)\right|$. As a result of this spurious peak, the application of Eq. 3 to $\mathscr{I}_\phi(k)$ leads to a residual grid pattern in the final SIM image (as is manifested in Figs. 3b and 3d).

Having isolated a cause of the residual grid pattern, a strategy to remove this pattern becomes clear. In particular, a high-pass filter can be applied to $\mathscr{I}_\phi(k)$ prior to the application of Eq. 3. The cutoff frequency of this high-pass filter should be high enough to eliminate most of the spurious peak about $k = 0$ while being low enough to perturb the remainder of $\mathscr{I}_\phi(k)$ as little as possible. It should be noted that the strategy presented in [23] of normalizing each raw image $I_1(x)$, $I_2(x)$ and $I_3(x)$ to its respective mean achieves a similar result, though it removes only the component of $\mathscr{I}_\phi(k)$ at exactly $k = 0$ while retaining residual components in the vicinity of $k = 0$. In other words, the removal of the spurious peak by normalization is incomplete. Examples of the results of narrow, sharp high-pass filtering where only the $\mathscr{I}_\phi(k = 0)$ component is removed versus broader high-pass filtering adjusted to the width of the spurious peak about $k \approx 0$ are illustrated in Fig. 5. The residual grid pattern is still apparent in Fig. 5a (although improved with respect to Fig. 3d), while it is manifestly eliminated from Fig. 5b. Moreover, the contrast, background rejection, and overall appearance of Fig. 5b have been visibly improved.

Some comments are in order. First, the question arises as to why phase stepping applied to out-of-focus background might be inaccurate in the first place. Many possibilities can account for this. For example, phase stepping is inaccurate if the out-of-focus backgrounds in images $I_1(x)$, $I_2(x)$ and $I_3(x)$ exhibit local inhomogeneities in fluorescence brightness that vary between raw images. This can be caused by grid-phase-dependent variations in the local illumination power delivered to the out-of-focus caused by inhomogeneities in the fiber core density or by sample-induced scattering or aberrations. Given a preponderance of out-of-focus background when imaging thick tissue samples, such variations need only be slight to provoke visible artifacts. Moreover, because our illumination source is coherent, we further expect that the in-focus grid pattern becomes deteriorated out of focus and more closely resembles speckle [25, 26, 27], in turn exacerbating the problem of random illumination inhomogeneities. In principle, the problem of out-of-focus speckle can be mitigated with the use of a rotating diffuser in the illumination path, however it cannot be removed altogether without considerable time averaging. It should also be be mentioned that a portion of the spurious peak at $\mathscr{I}_\phi(k \approx 0)$ can also arise from inaccurate phase stepping of the in-focus light (as opposed to the out-of-focus light), again possibility due to inaccurate grid periodicity caused by inhomogeneities in the fiber-bundle core distributions or sample-induced aberrations. However given the dominance of out-of-focus background over in-focus signal in the raw images apparent in Fig. 4d, this last possibility is likely to play a lesser role. In any event, the key point of applying a high-pass filter to $\mathscr{I}_\phi(k)$ is to remove the effect of inaccurate phase-stepping regardless of its source.

As a second comment, the application of a high-pass filter to $\mathscr{I}_\phi(k)$ is tantamount to correcting for intensity variations between the raw images locally rather than globally. When this high-pass filter is combined with the low-pass filter described above to eliminate spatial frequency components beyond the Nyquist cutoff, the net result is a bandpass filter very similar to what was referred to as wavelet prefiltering, which was previously applied to dynamic speckle illumination microscopy [28].

Finally, it should be cautioned that the strategy of applying a high-pass filter to $\mathscr{I}_\phi(k)$ should be used with care. This strategy is particularly effective when applied to thick tissue imaging which exhibits significant out-of-focus background. It becomes less effective, however, when applied to thin samples, particularly samples that exhibit spatial frequencies much higher than the grid frequency. In this last case, our strategy runs the risk of introducing spurious ringing in the proximity of sharp edges in the sample. In practice, we have found that it is best to adjust the cutoff frequency of our high-pass filter depending on the sample in question.

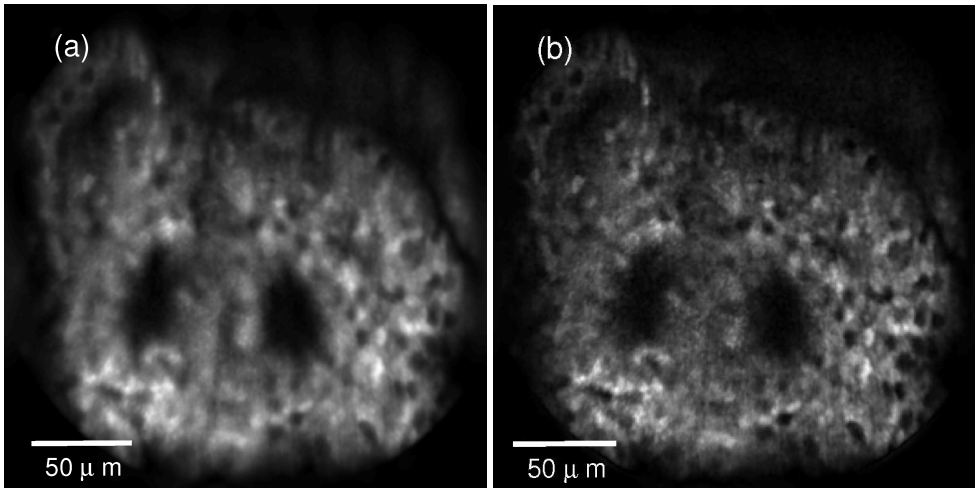

Fig. 5. (a) SIM image of rat colonic mucosa (same sample as in Fig. 3c-d) when each raw image is normalized to its respective mean. Note: this technique only partially suppresses the residual grid pattern in Fig. 3d. (b) SIM image using the technique of high-pass filtering of $\mathscr{I}_\phi(k \approx 0)$ to minimize the effects of imperfect phase stepping. Image quality is manifestly improved.

5. Conclusion

In conclusion, we have demonstrated the implementation of SIM with a flexible imaging fiber bundle appropriate for fluorescence endomicroscopy. Our final image resolution is on the order of 2.6μm, limited by the Nyquist frequency associated with the quasi-periodic core separation in the fiber bundle, over a field of view of about 240μm. In addition, we have described a strategy to largely suppress artifacts that result from inaccurate phase stepping. This strategy is found to be particularly beneficial when imaging thick samples that exhibit significant out-of-focus background. Such samples are of the type likely to be encountered when performing endomicroscopy in vivo. To our knowledge, our results represent the first demonstration of endomicrosopy with SIM, which we hope will have a broad impact in the biomedical community.

Acknowledgment

This work was funded by the Wallace H. Coulter Foundation. Tim Ford was supported by an NSF Research Experiences for Undergraduates (REU) award. The authors thank Satish Singh for help on the preparation of colon tissue samples, and Mauna Kea Technologies for assistance with the fiber probe design. Cathie Ventalon's current address is Neurophysiology and New Microscopies Laboratory, University Paris V, France.